ACS OMEGA

Open Access

http://pubs.acs.org/journal/acsodf

Article

Improvement of Intracellular Interactions through Liquid Crystalline Elastomer Scaffolds by the Alteration of Topology

Mahshid Fallah-Darrehchi and Payam Zahedi*

Cite This: *ACS Omega* 2023, 8, 46878−46891

Read Online

ACCESS | Metrics & More | Article Recommendations | Supporting Information

ABSTRACT: Preparation of inherently bioactive scaffolds has become a challenging issue owing to their complicated synthesis and nonrobust modified cell-actuating property. Liquid crystalline elastomers (LCEs), due to their combined specialties of liquid crystals and elastomers as well as their ability to respond to various kinds of stimuli, have reversibly led to the design of a new class of stimuli-responsive tissue-engineered scaffolds. In this line, in the first stage of this research work, synthesis and evaluation of acrylate-based LCE films (LCE^{film}) encompassing mesogenic monomers are carried out. In the second step, the design of an affordable electrospinning technique for preparing LCE nanofibers (LCE^{fiber}) as a problematic topic, thanks to the low molecular weight of the mesogenic chains of LCEs, is investigated. For this purpose, two approaches are considered, including (1) photo-cross-linking of electrospun LCE^{fiber} and (2) blending LCE with poly(ε-caprolactone) (PCL) to produce morphologically stable nanofibers ($PCL\text{-}LCE^{fiber}$). In the following, thermal, mechanical, and morphological evaluations show the optimized crosslinker (mol)/aliphatic spacer (mol) molar ratio of 50:50 for LCE^{film} samples. On the other hand, for LCE^{fiber} samples, the appropriate amounts of excessive mesogenic monomer and PCL/LCE (v/v) to fabricate the uniform nanofibers are determined to be 20% and 1:2, respectively. Eventually, PC12 cell compatibility and the impact of the liquid crystalline phase on the PC12 cell dynamic behavior of the samples are examined. The obtained results reveal that PC12 cells cultured on electrospun $PCL\text{-}LCE^{fiber}$ nanofibers with an average diameter of ∼659 nm per sample are alive and the scaffold has susceptibility for cell proliferation and actuation because of the rapid increase in cell density and number of singularity points formed in time-lapse cell imaging. Moreover, the $PCL\text{-}LCE^{fiber}$ nanofibrous scaffold exhibits a high performance for cell differentiation according to detailed biological evaluations such as gene expression level measurements. The time-lapse evaluation of PC12 cell flow fields confirms the significant influence of the reprogrammable liquid crystalline phase in the $PCL\text{-}LCE^{fiber}$ nanofibrous scaffold on topographical cue induction compared to the biodegradable PCL nanofibers.

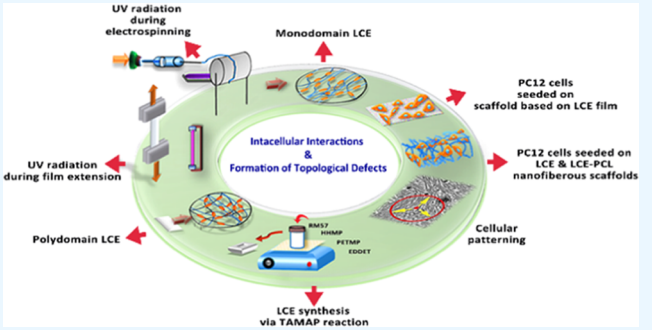

1. INTRODUCTION

The significance of polymeric biomaterials for tissue engineering is not deniable. In this line, a great deal of attempts have been focused on production of different in vitro environments that are able to provide efficient cell−cell and cell−scaffold interactions because the efficient and enough interactions lead to regeneration of target tissue similar to native tissue with optimal cost and time as well as simple operation conditions.[1,2]

Among various polymers, liquid crystalline elastomers (LCEs) are an emerging functional material that exhibits large and reversible shape deformations against external stimuli. This property makes them suitable for in vivo biological conditions in which external stimuli and dynamic deformations are effective factors for their regeneration procedure. LCEs have enabled an attractive balance between liquid crystalline polymers containing unfixed linear polymer chains and liquid crystalline thermosets comprising a highly cross-linked network. The position of aliphatic spacers in LCEs is such that they separate mesogens from each other and the polymer chain, leading to semiflexibility and minimum interactions between mesogenic units. The other influential characteristic of LCEs is their lightly cross-linked structure, providing a stabilized configuration, responsiveness to stimuli, and reversible shape deformation.[3−6]

In the past, synthesis approaches of LCEs were not relatively affordable; however, newly developed techniques based on click chemistry represent energy-efficient ways, including thiol−acrylate, thiol-epoxy, radical-mediated, thiol−ene, and thiol−yne. Thiol−acrylate Michael addition polymerization (TAMAP) is one of the mostly used methods to fabricate LCE

Received: August 31, 2023
Revised: October 23, 2023
Accepted: November 15, 2023
Published: November 29, 2023

Table 1. Amounts of Molar and Weight Ratios of the Reactants via TAMAP Reaction for LCE^{film} and LCE^{fiber} Samples

sample (cast films)	PETMP/EDDET (mol/mol)	sample (fibrous LCEs)	RM 257/EDDET (mol/mol)	sample (fibrous PCL-LCE)	PCL/LCE (v/v)
LCE_1^{film}	15:85	LCE_1^{fiber}	1.10:1	PCL-LCE^{fiber} (1:3)	1:3
LCE_2^{film}	25:75	LCE_2^{fiber}	1.15:1	PCL-LCE^{fiber} (1:2)	1:2
LCE_3^{film}	50:50	LCE_3^{fiber}	1.2:1	PCL-LCE^{fiber} (1:1)	1:1
LCE_4^{film}	75:25	LCE_4^{fiber}	1.25:1	PCL-LCE^{fiber} (2:1)	2:1
LCE_5^{film}	100:0				

scaffolds, which is a fast rate reaction and can be tailored by chain extenders and cross-linker amounts. Also, TAMAP reaction benefits from mild reaction conditions, minimal byproduct formation, high functional group tolerance, and high conversions when optimized.[7] Because of the aforementioned merits, this class of polymer materials has an indispensable role in biomimetic designs that are capable of manipulation for regulating biological functions.[1,8]

Anisotropic essence, quasi-liquid crystalline behavior, and responsiveness to liquid crystal induced topographical signals are highly evaluated properties of biological cells, confirming the similarity of LCEs with the biophysical nature of cells.[9,10] Active nematic theory and materiobiology are outstanding protectors for the development of scaffolds based on LCEs and for interpretation of the interplay between LCE scaffolds' surface topography and cellular topology.[11−13] It is noticeable that the liquid crystalline properties of various cell lines, including fibroblast cells,[14] muscular cells,[12,15] epithelial cells,[16,17] nerve cells,[18,19] and cancer cells,[20] have been investigated via recognition of singularity points, type of topological defects, displacement and velocity of defects, orientation of cells, and their strain rate. In the following, the cell viability of LCE scaffolds, possessing different topologies, has been evaluated more macroscopically and at the molecular level. The muscle-like behavior of LCEs directed researchers' interest toward the evaluation of muscular cell interactions with LCE-based scaffolds.[12,21] It is noticeable that nerve cells' response is highly dependent on scaffold-induced topographical signals, and failure to recreate the anisotropic architecture of nerve cells is a limitation in clinical repair. Despite the vague mechanism of nerve cells' reaction to the topography of patterned scaffolds, it has been confirmed many times that they are more compatible with three-dimensional (3D) platforms possessing anisotropic structure to resemble the native extracellular matrix, confer cell orientation, and guide axon growth and reconnection.[22,23] Recently, Ustunel et al. investigated the growth, proliferation, vascularization, and intercell communication of SH-SY5Y cells cultured on a caprolactone-based elastomer and LCE scaffolds. They found out that the intrinsic responsiveness and anisotropy of LCE scaffolds led to more improvement in maturation and differentiation of neuroblasma cells compared to caprolactone-based elastomers without liquid crystalline moieties.[2]

Depending on the type of application, LCEs in various morphologies, including 3D foams, cast films,[24,25] spherical particles,[26] and fibrous topology,[27,28] have been evaluated. Indeed, applying a methodology to control the molecular orientation and tailor the response to various external stimuli is a challenging issue. In most cases, the LCE is produced by injection of slightly cross-linked LCE between parallel glasses with predefined orientation along with ultraviolet (UV) exposure to stabilize the mesomorph of LCE. It is worth noting that there have been a few studies reporting the formation of LCE fibers via various and relatively problematic methodologies. The direct ink write printing approach is an extrusion-based layer-by-layer deposition of shape-shifting polymers recently approved due to its capability to produce aligned LCE fibers. In this method, an imposed driving force by the movement of the nozzle in the extruded printing process is able to align the mesogenic units of LCE and the obtained fibers are fixed substrates followed by the second stage of photo-cross-linking of LCE to stabilize the orientation of mesogens.[27,29−31] Wet spinning by a microfluidic device,[32,33] melt spinning,[27] and electrospinning[28,34−36] are the other types of methods that have been utilized to fabricate fibrous LCE. Among these methods, the electrospinning process with adjustability of operation conditions to obtain fibers with desired morphological properties and diameter is more preferable for developing LCEs. Since LCEs only swell and are not able to dissolve, the electrospinning of non-networked LCEs along with photo-cross-linking of deposited fibers or fabrication of core−sheath fibers via electrospinnable polymers as a support can be influential to facilitate the electrospinning of LCEs.

The new aim of the present study is to synthesize reprogrammable LCE scaffolds by the TAMAP approach to investigate the effect of intrinsic topographical properties of the liquid crystalline phase on the cell−cell and cell-scaffold interactions of PC12 cells. Therefore, the role of topology in bio-active LCE scaffolds and the effect of PCL as the topological support are quatitatively examined on LCE cast films and electrospun nanofibers based on LCE and PCL-LCE blend.

2. MATERIALS AND METHODS

2.1. Materials. RM 257 (1,4-Bis-[4-(3-acryloxypropyloxy)-benzoyloxy]-2-methylbenzene, white powder, molecular weight 588.60 g/mol) as mesogenic monomer was supplied by Merck (Wilshire Technologies Inc., Germany). EDDET (2,2-(ethylenedioxy) diethanethiol, transparent liquid, molecular weight 182.30 g/mol) as aliphatic spacer, PETMP (pentaerythritol tetrakis (3-mercaptopropionate), transparent viscous liquid, molecular weight 488.66 g/mol) as tetrafunctional mesogenic cross-linker, HHMP (2-hydroxy-4-(2-hydroxyethoxy)-2-methylpropiophenone, white powder, molecular weight 224.25 g/mol) as the photoinitiator of the second stage of the cross-linking reaction, DPA (dipropylamine, transparent liquid), a liquid catalyst for TAMAP reaction, and PCL (poly(ε-caprolactone), biodegradable polymer, average molecular weight 90 kg/mol) were provided from Sigma-Aldrich Co., Pillsburgh, The Netherlands. All of the other chemicals were analytical reagent grade and used without further purification.

2.2. Preparation of LCE Films (LCE^{film}). The synthesis approach of LCE samples was based on the TAMAP reaction including two stages:

2.2.1. Base-Catalyzed Radical Polymerization of Diacrylate Mesogenic Monomers and a Dithiol Monomeric Unit.

https://doi.org/10.1021/acsomega.3c06528
ACS Omega 2023, 8, 46878−46891

RM 257 as a monomeric component of the polymerization reaction was weighed according to the stoichiometric molar ratios represented in Table 1 and then, the predetermined amounts were inserted into glass vials (10 mL). Subsequently, toluene as the reaction medium with the weight ratio of toluene/RM 257 being 4:10 was added to the vials, and the mixtures were heated for 5 min at a temperature of 80 °C until homogeneous and transparent solutions were obtained. The obtained solutions were cooled to room temperature, while no monomeric recrystallization occurred. Following this, weighed amounts of PETMP and EDDET were added to the system, and then HHMP was immediately dissolved in the vials in the dark to prevent photo-cross-linking initiation at this stage and preserve it for the second stage of the photo-cross-linking reaction. Finally, after the addition of diluted DPA $\left(\frac{\text{DPA}}{\text{toluene}}(\text{v/v}) = \frac{1}{50}\right)$, the solutions were mixed by vortexing. The mixtures were transferred into the desired mold, and the polymerization reaction was continued in an oven at room temperature for 24 h without light. After the completion of the polymerization reaction, the molds were placed in a vacuum chamber for 12 h at a temperature of 60 °C and a pressure of 508 mmHg to evaporate the residual toluene. The product of this stage was the polydomain weakly cross-linked LCE.

2.2.2. Photo-Cross-Linking of LCE. In order to determine an alignment and orient the mesogenic units parallel to director vector , the LCE samples were strained up to two times their initial length with an extension rate of 120 mm/min. The applied strain (50 and 100%) at the determined loading caused alignment of polymer chains and mesogenic units. The oriented conformation of LCE was chemically stabilized via the photoinitiated cross-linking reaction, in which the strained samples were exposed to an ultraviolet (UV) light source with a wavelength of 362 nm and power of 10 W at a distance of 10 cm for 10 min.

2.3. Preparation of LCE Fibrous Samples (LCE$^{\text{fiber}}$). To prepare the electrospinning solution, firstly, the solutions were prepared according to Table 1 without the cross-linker (PETMP) and in the presence of excessive RM 257 in the range of 10−25%. Also, chloroform was considered as the solvent medium due to its faster evaporation rate and higher polarity compared to toluene. It should be noted that the samples should be kept in the sealed flask for 24 h at a room temperature of 25 °C to complete the first stage of the TAMAP reaction. Then, the samples were inserted into aluminum-covered syringes for light prevention. The operational conditions for the electrospinning process were determined in such a way that all of the samples could easily come out of the syringe pump, the solution would not be clotted, and the process would not be stopped during fiber production. To fabricate the LCE fibrous samples, an electrospinning device (model eSpinner NF-CO EN/II, Asian Nanostructure Technology Co., Tehran, Iran) was utilized. During the electrospinning process, the LCE solutions were injected at a constant flow rate (0.45 mL·h^{-1}) by using a syringe micropump alongside a high voltage (20 kV) and a needle tip to collector distance of 14.5 cm, as well as the formed fibers were collected on a drum. During this procedure, UV light was inserted along the pathway of the fiber formation from the needle tip to the collector at a distance of 10 cm. During the electrospinning process, the superficial tension, superficial extensile stress originated from a high-voltage electric field, and rotation of the collector led to oriented mesogenic units. The orientational order was stabilized by the second stage of photo-initiated cross-linking of oligomeric chains, and continuous fibers were collected on the rotating drum. Finally, LCE-fiber samples were removed from the collector and inserted into the vacuum chamber at a temperature of 60 °C to evaporate the trapped moisture or residual solvent.

2.4. Preparation of Electrospun PCL and PCL-LCE Nanofibrous Samples (PCL-LCE$^{\text{fiber}}$). In order to produce the electrospun PCL nanofibrous sample, first, the PCL solution was prepared by gradual addition of weighed PCL (1.1 g) to the solvent mixture (chloroform/dimethylformamide in the ratio 7:3 (v/v)). PCL granules were dissolved by stirring at ambient temperature for 2 h until the homogeneous solution was obtained. Nanofibrous samples were prepared by utilizing the electrospinning device and the optimized operational conditions were as follows: solution flow rate 0.45 mL h $^{-1}$, applied voltage 19.5 kV, and the distance between the syringe needle tip and collector 14.5 cm.[37] In the following, in order to obtain nanofibers based on PCL-LCE, oligomeric solutions were prepared based on the optimized LCE sample (Section 2.2) and were homogeneously mixed with PCL in various volume ratios (Table 1).

2.5. Fourier Transform Infrared Spectroscopy. Fourier transform infrared spectroscopy (FT-IR, Spectrum Two, PerkinElmer Inc.) was utilized to investigate and compare the functional groups in the LCE$^{\text{film}}$, LCE$^{\text{fiber}}$, and PCL-LCE$^{\text{fiber}}$ samples. Also, for evaluation of newly formed bonds via the reaction of thiol−acrylate groups as well as photo-cross-linking of LCE, FT-IR spectra were required. The test was done at wavenumbers ranging from 400 to 4000 cm^{-1} using a potassium bromide tablet for the sample preparation at a resolution of 100 scans.

2.6. Differential Scanning Calorimetry. For observation of the transition temperatures and measurements of the thermal properties of the samples, differential scanning calorimetry (DSC, 200 F3Maia, NETZSCH-Kunststof Co., Selb, Germany) was utilized. This test was used to study the melting process of the crystalline structures and their glass transitions as well as nematic−isotropic transition temperatures (T_g and T_{NI}). The samples with a weight of about 17 mg were heated to 120 °C at a rate of 5 °C/min.

2.7. Dynamic Mechanical Thermal Analysis. A dynamic mechanical thermal analyzer (DMTA, Tritec 2000, Triton Technology, England) was employed to determine the viscoelastic properties and shape the memory performance of the prepared samples. In this test, the samples with dimensions of 20 × 10 × 1 mm^3 were placed in a chamber, and the test was performed with a frequency of 1 Hz as well as amplitude of 0.1% with the temperature ranging from −30 to +90 °C. The analysis was utilized to evaluate the ability of the samples to fix the temporary shape (fixity) and the changes in tan δ and T_g as a function of the structural features. The fixity ratio was measured using eq 1 to examine the shape memory of samples

$$\text{fixity ratio (\%)} = \frac{\varepsilon_{\text{fixed}}}{\varepsilon_{\text{applied}}} \times 100 \quad (1)$$

where "$\varepsilon_{\text{fixed}}$" and "$\varepsilon_{\text{applied}}$" are the permanent strain after photo-cross-linking and stretch of the sample before photo-cross-linking, respectively.

2.8. Cross-Link Density. The cross-link density (CLD) was calculated using Flory−Rehner equation eq 2

https://doi.org/10.1021/acsomega.3c06528
ACS Omega 2023, 8, 46878−46891

Table 2. Primers for Specific Differentiation Genes Used in qRT-PCR

gene	sequence (from 5′ to 3′)	length	ref
Nestin	F: CCAAGCAGGTGAACAAGACTCC	98bp	NM_001308239.1
	R: GGTCCTCTAGCCCTACCACT		
Map2	F: TGGCTCTCTAAAGAACATCCG	60bp	NM_013066
	R: TTGGCTGTCAATCTTCACGTT		
Tubb3	F: GCCACCTTTGTATTTATGTTGC	111bp	NM_139254.2
	R: CCCCTCCAAATATAAACACAACC		
Hprt1	F: GGTTCTGTCATGTCGACCCTC	122bp	NM_012583.2
	R: CCTTCATGACATCTCGAGCAAG		

$$\upsilon = \frac{-[\ln(1 - V_r) + V_r + \chi V_r^2]}{V_0(V_r^{1/3} - 0.5\, V_r)} \quad (2)$$

where "υ" represents the CLD and "V_0", "χ", and "V_r" denote the molar volume of the solvent, polymer/solvent interaction parameter, and volume fraction of the LCEs in the swollen state, respectively.

2.9. Wide-Angle X-ray Scattering. The samples were analyzed by wide-angle X-ray scattering (WAXS, 3710, Philips Co., Netherlands) associated with Cu Kα radiation (40 kV, 30 mA) operated in a step-scanning mode over a 2θ range of 10−100° with a step width of 0.02° and a count time of 1 s per step. The distance between crystal layers (d) in the LCE samples was obtained by using Bragg's equation eq 3

$$n\lambda = 2d\sin(\theta) \quad (3)$$

where "θ" is the angle between the incident ray and the scatter plane, "λ" is the wavelength of the X-ray radiation, and "n" is an integer, which is usually considered to be 1.[38]

Furthermore, the degree of crystallinity (%C) was calculated based on eq 4

$$\%C = \frac{A_{cry}}{A_{cry} + A_{am}} \times 100 \quad (4)$$

where "A_{cry}" is the area under the peak of the crystalline part and "A_{am}" is the area under the peak in the amorphous part of the diffraction pattern.

For each sample, the order parameter (S) was determined using the X-ray diffraction (XRD) diagram and integration of the enclosed surface eq 5.

$$S = \frac{\int_0^{\pi/2} I_{(\alpha)} \frac{3\cos^2\alpha - 1}{2} \sin\alpha \, d\alpha}{-\frac{1}{2}\int_0^{\pi/2} I(\alpha)\sin(\alpha)\, d\alpha} \quad (5)$$

where S is the scalar order parameter, α is the azimuthal angle, and the normalized amplitude for the total intensity is written in terms of azimuthal intensities, I (α), collected from the diffraction pattern.

2.10. Mechanical Properties. The effect of UV irradiation on the mechanical properties of the LCE^{film} samples, comparing the mechanical properties of film and fibrous samples, was evaluated using a universal tensile instrument (5566, Instron, England). The specimen used for testing was 30 mm in length, 5 mm in width, and 0.5 mm in thickness.

2.11. Polarized Optical Microscopy. The LCE mesomorphic properties were observed using polarizing optical microscopy (POM, BX53-P, Olympus, Japan). The results of this test revealed the changes of the nematic−isotropic phases as a function of temperature, especially T_{NI}.

2.12. Field Emission Scanning Electron Microscopy. The morphology observations of the samples were carried out using a field emission scanning electron microscope (FE-SEM, SU8040, Hitachi, Japan) at 20,000× magnification. Prior to the FE-SEM test, all of the samples were sputtered with a thin layer of gold using an auto-sputter coater (model E5200, Bio-Rad, United Kingdom).

2.13. Optical Microscopy. The stained PC12 cells were observed by an optical microscope (OM, BX-51, Olympus, Japan) with a scale bar of 50 μm.

2.14. Cell Cultures. In this study, the adrenal phaeochromocytoma (PC12) cell line provided from Pasteur Institute, Tehran, Iran, was cultured in Dulbecco's Modified Eagle Medium (DMEM, D5796; Sigma-Aldrich, St. Louis, MO) containing 10% fetal bovine serum and 1% penicillin-streptomycin (P4333; Sigma-Aldrich, St. Louis, MO). The cells were then incubated in 5% CO_2 at 37 °C for 24 h; then, the medium was changed to the differentiation media containing DMEM and 2% horse serum (Thermo Fisher Scientific, MA).

2.14.1. Cell Viability. The cells in the confluence of 80−90% were plated in 96-well plates. The cell density for cytotoxicity assays was 5×10^3 cells/well. Then, the cells were cultured on different synthetic substrates of LCE^{film}, LCE^{fiber}, and PCL-LCE^{fiber} samples. The plates were incubated for 24 h until the cells adhered to each well substrate. After 24 and 48 h, 10 μL of 3-(4,5-dimethylthiazol-2-yl)-2,5-diphenyltetrazolium bromide (MTT) solution (0.5 mg/mL in phosphate-buffer saline (PBS), DNAbiotech, South Africa) was added to each well; the microplates were incubated at 37 °C for 4 h, protected from light, to observe the presence of formazan crystals. Next, the media were removed, the wells were gently filled with 100 μL of dimethyl sulfoxide, and the absorbance was read at 570 nm.

2.14.2. Flow Cytometry. 5×10^5 PC12 cells were seeded per well in a 6-well plate, and after 1 day the cells were detached and seeded on the synthesized substrates. After 36 h, the cells were detached and washed with PBS and subsequently stained with Nestin Polyclonal Antibody (BS-0008R, Bioss) at room temperature for 20 min. Next, the cells were incubated with FITC Donkey antirabbit IgG Antibody (406403, Biolegend) for 20 min in the dark. The samples were analyzed by flow cytometry (Partec, Cyflow, Germany). For each experiment, 20,000 events per sample were read. All data were analyzed with FlowJo software version 7.6.5.

2.14.3. Immunocytochemistry Staining of Nestin. Cells were seeded on sterile glass slides to visualize the shape of actins by fluorescence microscopy. The 4% (v/v) formaldehyde used to fix the cells was used for the staining. The nucleus was stained using 3 mg/mL 4,6-diamidino-2-phenylindole hydrochloride (DAPI, Sigma-Aldrich, St. Louis, MO)

https://doi.org/10.1021/acsomega.3c06528
ACS Omega 2023, 8, 46878−46891

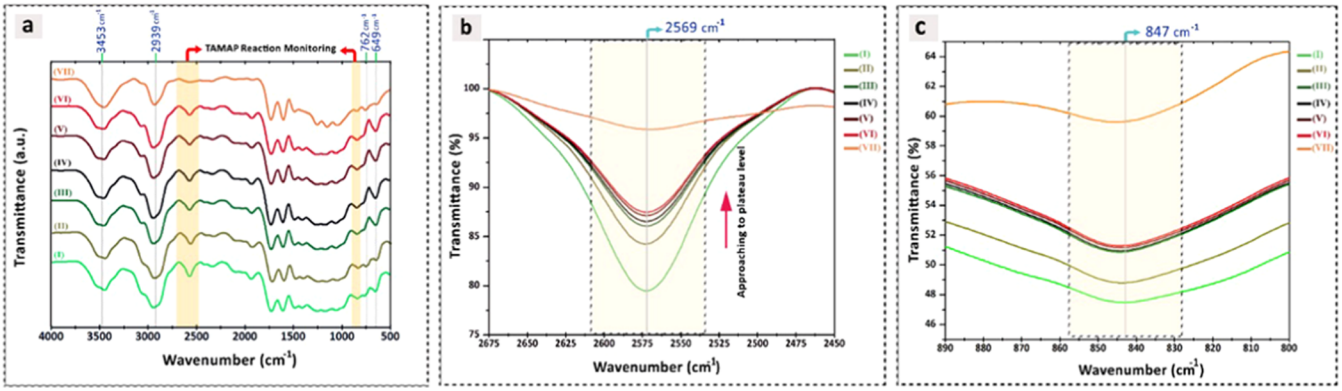

Figure 1. (a) FT-IR spectra for time-dependent monitoring of TAMAP reaction, (b) change in intensity of the thiol functional groups' characteristic peaks by time, and (c) the sharpness reduction of acrylate functional groups in 30 min.

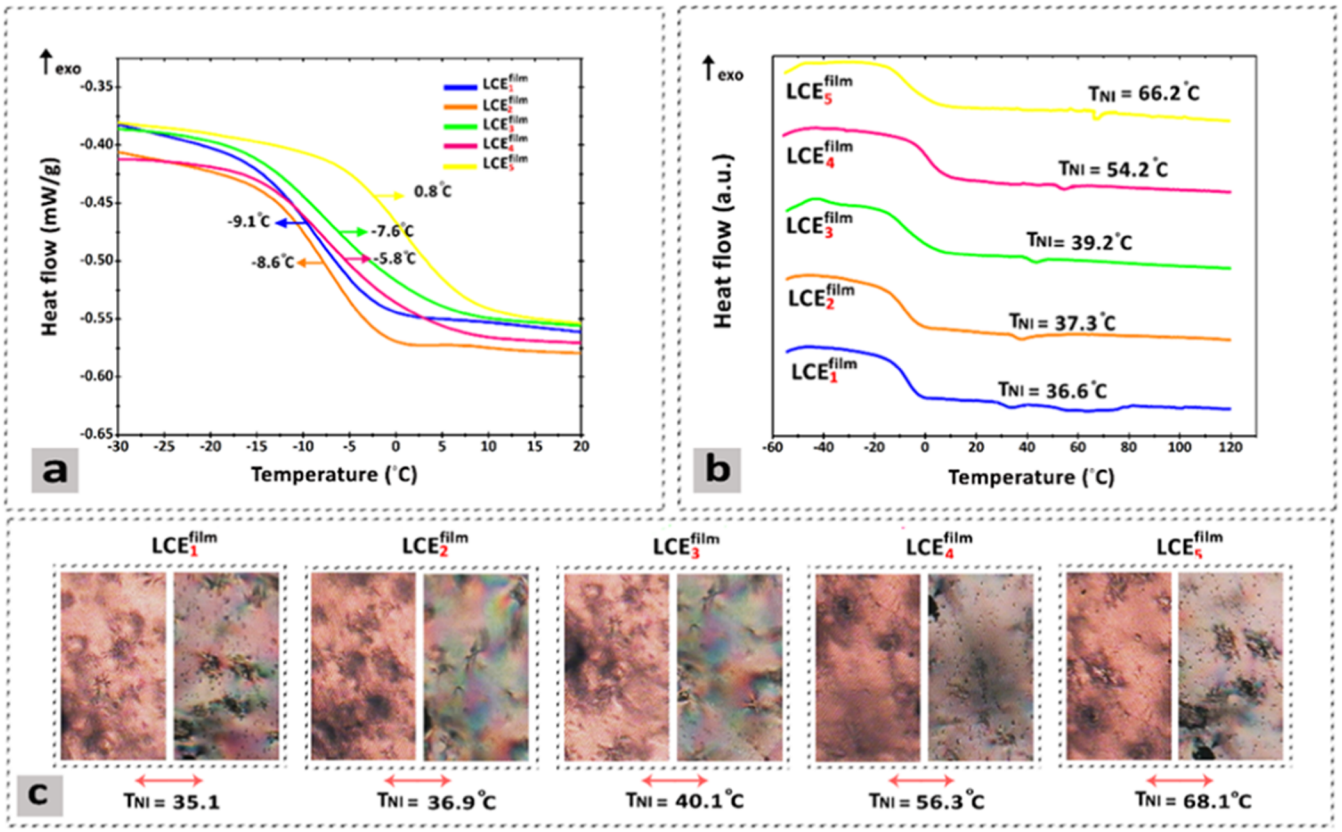

Figure 2. (a) DSC thermograms indicating the T_g for LCE^{film} samples, (b) DSC thermograms showing the T_{NI} for LCE^{film} samples, and (c) POM images depicting the phase transition at T_{NI} for LCE^{film} samples.

incubated in darkness for 10 min. Images were captured using an Olympos-20 × 51 microscope coupled to a DP71 camera.

2.14.4. Real-Time PCR. Gene expression levels were determined using RT-PCR after 4 days of culture. Total RNA was isolated using the Qiagen RNeasy Mini Kit, according to the product's datasheet. RNA was retrotranscribed with a cDNA Reverse Transcription Kit (Thermo Fisher Scientific) using 300 ng of RNA followed by DNase I treatment (3.1.21.1, Amplification, Millipore Sigma Co.). Gene expression quantitative analysis was performed using SYBR Green Master Mix (RR82LR, TAKARA, Japan) in a ROTOR GENE Real-Time PCR device (QEC21313, QIAGENE). The primers for the differentiation genes are given in Table 2. Hprt1 was used as an internal control gene for data analysis because of its constant value of gene expression among samples.

2.14.5. Cell Counting Kit 8 Assay. PC12 cells were seeded in a 24-well plate at a density of 8 × 10^3 cells/well in control, LCE_3^{film}, UV-radiated LCC_3 (UV-R LCE3), LCF_4, PCL_1-LCE_3, and (UV-R LCE3) groups. At 0, 24, 48, and 72 h, the cell proliferation activity was detected using the CCK8 assay [Abcam (ab228554), MA]. In brief, the medium was replaced with fresh medium containing 10% CCK8 solution, and the plate was incubated at 37 °C for 1 h. The absorbance at 450 nm was examined using a hybrid microplate reader (Synergy H4, Agilent BioTek, CA).

https://doi.org/10.1021/acsomega.3c06528
ACS Omega 2023, 8, 46878−46891

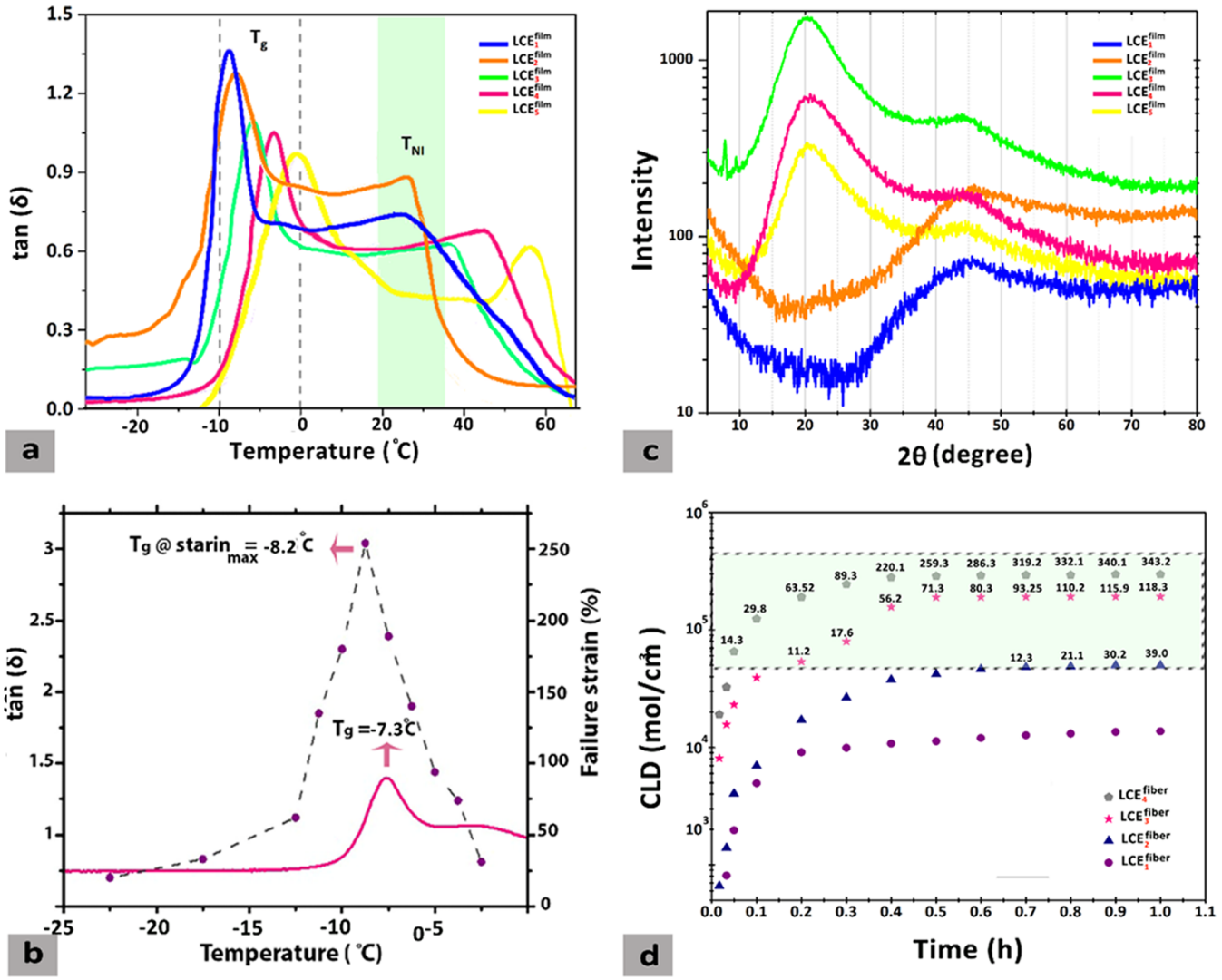

Figure 3. (a) DMTA analysis of LCE^{film} samples to observe transition temperatures, (b) tan (δ) and strain failure amounts versus temperature, (c) WAXS patterns of LCE^{film} samples to calculate the percentage of crystallinity and order parameter (S), and (d) diagram of CLD amounts versus time and tensile strength amounts (kPa) for nonsticky LCE^{fiber} samples.

3. RESULTS AND DISCUSSION

3.1. Time-Dependent Monitoring of TAMAP Reaction. The first stage of this study comprised preparation and characterization of LCE films, which were different in PETMP/EDDET (mol:mol) ratio. As mentioned earlier, the preparation of LCEs via TAMAP reaction is based on a two-phase cross-linking reaction. In order to monitor the cross-linking reaction during the polymerization of the mesogenic monomer and in the exposure of UV irradiation (362 nm, 8 W, distance of 15 cm), the reactants were dissolved in toluene, and formation of new functional groups and the rate of some characteristic peaks' disappearance were investigated. Figure 1a shows the FT-IR spectra of LCE samples denoted by (I), (II), (III), (IV), (V), (VI), and (VII), in which TAMAP for sample (I) without UV exposure proceeded for 15 min. In contrast, along with the TAMAP reaction, photo-initiated cross-linking reaction was carried out by the exposure of the other samples to the UV light with 5 min intervals' sample (II) for 5 min, sample (III) for 10 min, sample (IV) for 15 min, sample (V) for 20 min, sample (VI) for 25 min, and sample (VII) for 30 min. As depicted and highlighted, the characteristic peaks at 649 and 762 cm^{-1} were attributed to C−S and C−H bonds, respectively. The existence of C−S groups was due to the click reaction between acrylate and thiol groups. Also, the characteristic peak at the wavenumber of 2569 cm^{-1} was assigned to the unreacted thiol groups existing in EDDET and PETMP. As displayed in Figure 1b, with the reaction progressing, the peak intensity was reduced and the rate of reduction was intensified by the UV irradiation. Analyzing the thiol functional groups' characteristic peaks in EDDET from sample (I) to sample (VII) showed that their bonds reacted with the vinyl groups (C═C) in the diacrylate mesogenic monomer, thereby reducing the intensity of this peak while undergoing plateau. In other words, the maximum intensity was observed for sample (I), due to the absence of UV irradiation. The acrylate groups were also consumed over time from sample (I) to sample (VII), leading to the thiol−acrylate reaction and photo-cross-linking procedure. The second stage of cross-link formation was initiated by the UV irradiation toward acrylate groups followed by generating free radicals and cross-linking between the excessive acrylate groups in the monomer [Figure 1c]. Furthermore, the other peaks at the wavenumbers of 3453 and 2939 cm^{-1} assigned to the

https://doi.org/10.1021/acsomega.3c06528
ACS Omega 2023, 8, 46878−46891

stretching vibration of −OH and C−H bonds appeared owing to the adsorbed moisture and the aliphatic structure of RM 257, respectively.

3.2. Investigation of Transition Temperatures and Order Parameters. These materials were subjected to thermal analysis via DSC. As shown in Figure 2a, the T_g of the samples was increased from −9.1 to 0.8 °C, which could be because of the increase of PETMP amount, leading to the formation of a liquid crystalline cross-linked network. T_{NI}, another thermal transition temperature of the samples, appeared above ambient temperature, resulting in the samples being in anisotropic state [Figure 2b].[39] Moreover, the study of T_{NI} for each sample was also carried out via the POM images depicted in Figure 2c. In this line, the samples were heated at the heating rate of 5 °C/min and cooled to ambient temperature up to 120 °C to observe the nematic ↔ isotropic phase transition phenomenon. The obtained amounts of T_{NI} by the evaluation of images obtained from POM confirmed the accuracy of the measured amounts via DSC.

The DMTA results were also studied to confirm the DSC and POM obtained results.[39] As shown in Figure 3a, a bimodal tan δ peak corresponding to T_g and T_{NI} appeared possessing similar trends of DSC transition temperatures. The effect of cross-linking agent could be found from the changes of T_g and T_{NI} in the LCE^{film} samples because of the impact of cross-linking density on the mobility of the polymer chains. Additionally, as PETMP was decreased, the intensity of tan δ was continuously increased because of the LCE segments' movements followed by dynamic force dissipation. In this case, as seen in Figure 2b, the tan δ curve remained almost flat in the temperature range of T_g to T_{NI}, which was due to the stability of the liquid phase structure. The height of the flat region remained constant between the values of 0.46 and 0.84, indicating the consistency of the nematic phase state in the temperature range between T_g and T_{NI}. The cross-linking density (CLD) of LCEs is reported in Table 2. Accordingly, the CLD [$\nu \times 10^6$ (mol/cm^3)] values were decreased from 3.96 × 10^6 mol/cm^3 (LCE$_1^{film}$) to 15.40 × 10^6 mol/cm^3 (LCE$_5^{film}$). Also, the amounts of CLD were proportional to the contents of the cross-linker, which means that by increasing the CLD value, more restriction was applied to the segmental mobility of the LCEs^{film}.[40] Figure 3b depicts the WAXS patterns for LCE^{film} samples, of which some had a relatively broad peak at 2θ = 21.5°. For LCE$_5^{film}$, LCE$_4^{film}$, and LCE$_3^{film}$, 2θ = 41.6° for all fibrous samples. The WAXS patterns displayed a peak, in which the maximum intensity belonged to the LCE$_3^{film}$, which was attributed to the capability of this sample to form the ordered layers. The decrease in intensity of the LCE$_5^{film}$ compared to the LCE$_4^{film}$ sample affirmed the fact that the capability of mesogen to orient was substantially increased owing to its leveling up the freedom of movement. However, for the LCE$_3^{film}$ sample, the presence of PETMP led to a stabilized oriented topography of polymer chains along with suitable freedom of movement to form an ordered molecular organization. As can be seen in Table 3, on raising the PETMP amount, the D-spacing indicating the distance between the mesogenic core plates showed a trend similar to the trends of crystallinity percentages and order parameter (S) amounts. The percentage of crystallinity from LCE$_1^{film}$ to LCE$_5^{film}$ was firstly increased and reached an optimum amount (59.71%) for the LCE$_3^{film}$ and then decreased because the increase of PETMP amount to form an aligned topography at the molecular level. Also, the order parameter amount for LCE$_3^{film}$ proved that this sample was more capable of arranging the chains aligned.

Table 3. Amounts of CLD, Crystallinity, D-spacing, and Order Parameter for LCE^{film} Samples

sample (cast films)	$\nu \times 10^{-6}$ (mol/cm^3)	crystallinity (%)	D-spacing (deg)	S (order parameter)
LCE$_1^{film}$	3.96	39.61	4.16	0.215
LCE$_2^{film}$	6.32	40.23	4.33	0.361
LCE$_3^{film}$	9.61	59.71	4.32	0.468
LCE$_4^{film}$	12.15	38.65	4.31	0.145
LCE$_5^{film}$	15.40	41.6	4.20	0.268

3.3. Shape Memory and Thermoresponsiveness Properties of LCE^{film} Samples. In order to study the mechanical dynamic properties of LCE^{film} samples such as shape memory, the effect of PETMP and EDDET on these characteristics was studied using ten samples. Each LCE^{film} sample was subjected to two strains of 50 and 100% at the extension rate of 0.2 mm/s. They were exposed to UV irradiation with a wavelength of 365 nm and the intensity of 210 mW/mm for 10 min. The dimensions of the samples were measured before and after the stretched state. Then, the samples were placed in an oven with a temperature of 85 °C (higher than the transition temperature (T_{NI})), and the dimensions of the samples were measured again. By using eq 2 the fixity of each sample was measured (Table 4).

Table 4. Fixity Percentage for LCE^{film} Samples

sample	fixity (%)@strain of 100%	fixity (%)@strain of 50%
LCE$_1^{film}$	81.3	73.5
LCE$_2^{film}$	80.5	70.2
LCE$_3^{film}$	86.5	81.3
LCE$_4^{film}$	78.5	69.3
LCE$_5^{film}$	73.5	64.0

Evidently, all of the samples have the property of shape memory, and with the increase in the amount of strain during UV irradiation, the value of fixity increased in all the samples. Also, the LCE$_3^{film}$ sample had the highest amount of fixity. For a more detailed analysis, the strain failure diagram versus temperature in terms of percentage of PETMP for all samples is provided. The data related to the measurements of the failure strain for each sample showed that the LCE$_3^{film}$ sample had the highest amount of failure strain (259%). To check at what temperature the failure strain occurred for the LCE$_3^{film}$ sample, the failure strain along with the tan (δ) diagrams were plotted for this sample. The comparison of two graphs showed that the failure strain occurred at almost the same T_g as that of the mentioned sample.

Obtaining fibrous or especially nanofibrous topology by the electrospinning process is highly dependent on the polymer's molecular weight and the structure of the polymer as well as the polarity and viscosity of the polymer solution. Moreover, the weight-average molecular weights (M_w) of LCE samples were measured by the gel permeation chromatography method [Table S-1], indicating whether the sample is suitable for the electrospinning process. To stabilize the fibrous morphology, the approach of photo-cross-linking of mesogenic monomers using HHMP attack on excessive amounts of acrylate end groups of RM 257 was considered. In this line, first, the capability of LCE samples to produce a uniform fibrous

https://doi.org/10.1021/acsomega.3c06528
ACS Omega 2023, 8, 46878−46891

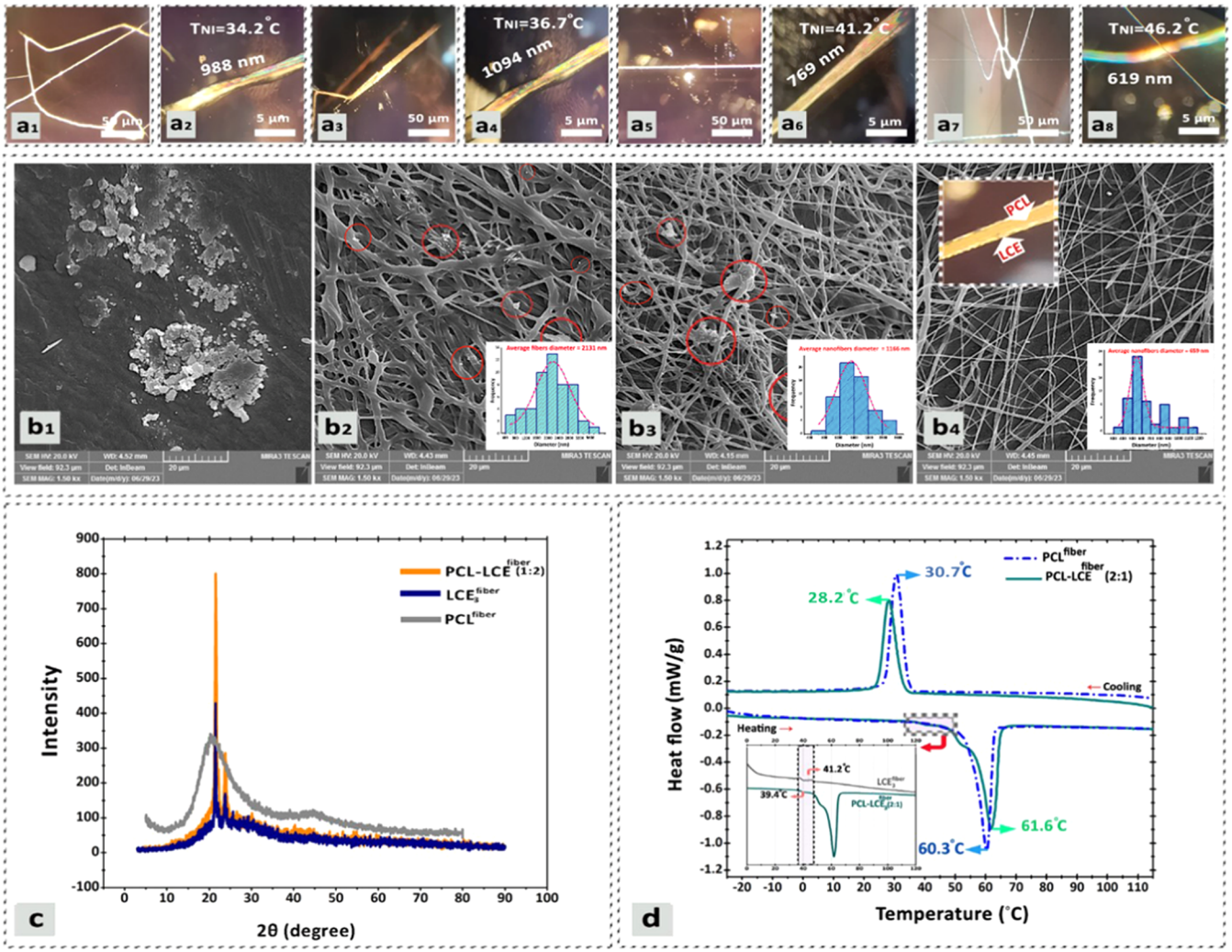

Figure 4. POM images of LCE ^{fiber} samples: (a_1) electrospun LCE_1^{fiber} (50 μm), (a_2) electrospun LCE_1^{fiber} (5 μm), (a_3) electrospun LCE_2^{fiber} (50 μm), (a_4) electrospun LCE_2^{fiber} (5 μm), (a_5) electrospun LCE_3^{fiber} (50 μm), (a_6) electrospun LCE_3^{fiber} (5 μm), (a_7) electrospun LCE_4^{fiber} (50 μm), and (a_8) electrospun LCE_4^{fiber} (5 μm). SEM micrographs of PCL- LCE_3^{fiber} nanofibrous samples: (b_1) PCL- LCE_3^{fiber} (1:3), (b_2) PCL- LCE_3^{fiber} (1:2), (b_3) PCL- LCE_3^{fiber} (1:1), and (b_4) PCL- LCE_3^{fiber} (2:1); (c) WAXS patterns for (b_1) PCL- LCE_3^{fiber} (2:1), PCL, and LCE_3^{fiber} and (d) thermograms (heating) for PCL^{fiber} and PCL- LCE_3^{fiber} (2:1).

morphology was investigated with various amounts of excessive monomer (Table 1).

3.4. Evaluation of the Mesophase and Morphology of LCE^{fiber}. To evaluate the effect of UV irradiation on the CLD values, tensile strength, fiber formation, and determination of electrospinning conditions, LCE^{fiber} samples were exposed to UV light (with wavelength 365 nm and intensity 210 mW/mm) for 1 h in a glass capillary with an inner diameter of 500 μm at the distance of 10 cm (these amounts were selected based on electrospinning conditions). The CLD values versus time were plotted for all samples, and tensile strength amounts for nonsticky specimens were measured (green area) [Figure 3d]. Measurements of minimum and maximum distances between the syringe pump and collector as well as the time required to obtain a morphologically stable fiber are shown in Figure 3d (flow rate = 0.45 mL/h, distance between the syringe pump and collector = 14.5 cm, voltage = 20 kV). The obtained morphologies displayed in Figure S-1 at voltages of 14, 17, and 20 kV confirmed that the optimized voltage was 20 kV.

To evaluate the morphological features of electrospun LCEs, the samples including LCE_1^{fiber}, LCE_2^{fiber}, LCE_3^{fiber}, and LCE_4^{fiber} were prepared with constant operation conditions. In order to observe the phase transition and morphology, the samples were observed via POM. As shown in Figure 4, the resultant electrospun samples were all bright between crossed polarizers, indicating the liquid crystalline phase with a nematic mesomorph. As seen, the samples were relatively the same in terms of morphology and average diameter. However, LCE_1^{fiber} and LCE_2^{fiber} mixtures, which contained 15 and 30% excessive mesogenic monomers, had a fibrous topology but they were sticky and nonuniform, without smoothness and a stable morphology [Figure 4a_1–a_4]. In other words, photo-cross-linking of the mentioned samples during the electrospinning process was not enough to produce a dimensionally robust fiber. Also, the final obtained fibrous media for these samples were sticky even after re-exposure to UV irradiation, which could be attributed to the insufficient CLD amounts shown in Table 1. In contrast, the prepared LCE_3^{fiber} and LCE_4^{fiber} samples were relatively uniform and smooth [Figure 4a_2,a_4]. Comparison of the LCE_3^{fiber} and LCE_4^{fiber} diameters showed

https://doi.org/10.1021/acsomega.3c06528
ACS Omega 2023, 8, 46878−46891

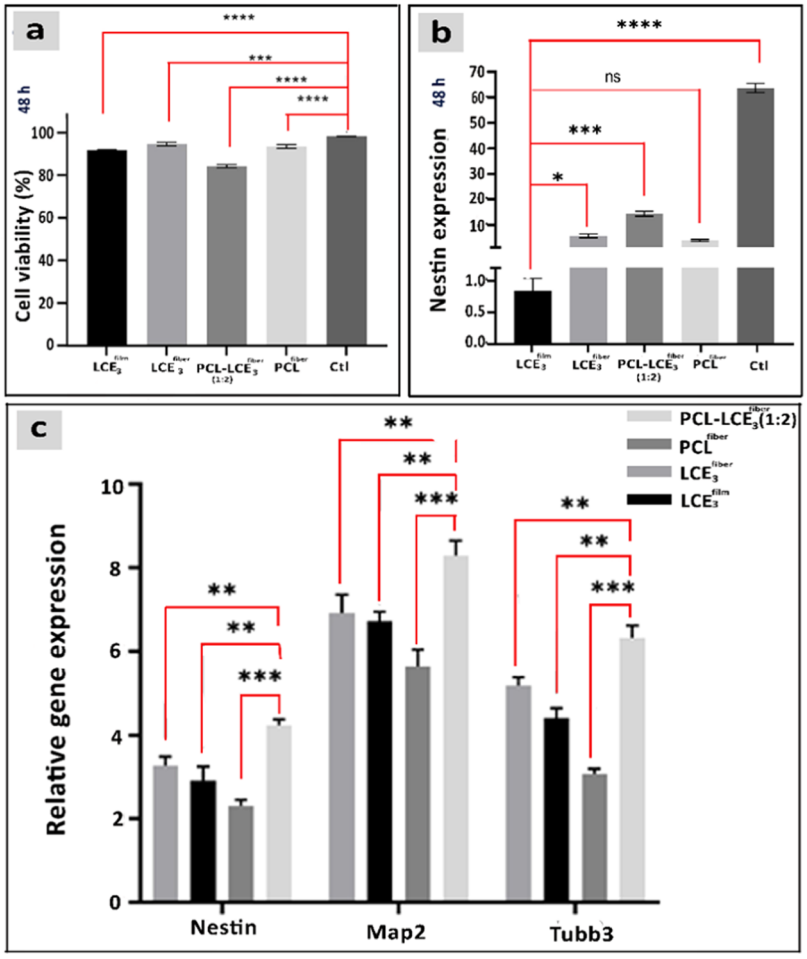

Figure 5. (a) Percentage of live cells cultured on LCE_3^{film}, LCE_3^{fiber}, and PCL- LCE_3^{fiber} (2:1), (b) Nestin expression of PC12 cells cultured on LCE_3^{film}, LCE_3^{fiber}, and PCL- LCE_3^{fiber}, and (c) expression of all neural differentiation gene markers, including Nestin, Map2, and Tubb3.

that increase in the amount of additional monomer led to a significant decrease in the fiber diameter compared to the other samples [Figure 4a_2,a_4,a_6,a_8]. Indeed, the rate of photo-cross-linking in LCE_1^{fiber} and LCE_2^{fiber} was much lower than that of samples including LCE_3^{fiber} and LCE_4^{fiber}. The other effective reason to confirm the suitability of LCE_3^{fiber} could be attributed to the M_w amounts of the samples proving that samples with higher M_w are more capable of producing electrospun nanofibrous topography, as confirmed in LCE_3^{fiber} and LCE_4^{fiber} due to their acceptable morphology.[3] In LCE_4^{fiber}, due to the high amount of excessive monomer, before reaching the collector, strands were cross-linked and it was not possible to create a fibrous network by the electrospinning process. Also, the photo-cross-linking of LCE_3^{fiber} started while the solution discharged. Investigation of the mechanical and morphological features and qualitative surface adhesion showed that the LCE_3^{fiber} sample had a suitable CLD value, being stable morphologically and structurally.

Also, the nanofibrous PCL-LCE_3 samples described in Table 1 were fabricated using an electrospinning device with the operation conditions as follows: flow rate = 0.45 mL h^{-1}, the distance between needle and collector = 14 cm, and applied voltage= 20 kV. As the above section confirmed that LCE_3^{fiber} fabricated via electrospinning along with photo-cross-linking procedures had more suitable morphological features, LCE_3^{fiber} was selected to blend with PCL. To select the optimum nanofibrous sample as a smart scaffold, PCL and LCE_3 were blended in different ratios (v/v), in which, for example, PCL-LCE_3^{fiber} (2:1) meant that the PCL solution volume is twice that of LCE_3. In this line, four PCL-LCE_3^{fiber} samples, including PCL-LCE_3^{fiber} (1:3), PCL-LCE_3^{fiber} (1:2), PCL-LCE_3^{fiber} (1:1), and PCL-LCE_3^{fiber} (2:1), were prepared and evaluated morphologically. Figure 4b_1,b_2 displays the SEM micrographs of the mentioned samples, which proved that LCE_3 presence decreased the density of electrospun fibers and electrospinnability. Figure 4b_1 confirmed that PCL-LCE_3^{fiber} (1:3) could not form a fibrous topology and the high amount of LCE_3 caused the formation of nonuniform photo-cross-linked agglomerates on PCL nanofibers. By comparing the micrographs in Figure 4b_3,4b_4, it could be concluded that photo-cross-linked LCE_3^{fiber} agglomerates decreased for lower LCE amount. Also, Figure 4b_1,b_2 reveals that in PCL-LCE_3^{fiber} (1:3) and PCL-LCE_3^{fiber} (1:2), the formed fibers were ribbon-like and nonuniform. In contrast, based on Figure 4b_3,4b_4, the prepared nanofibers were uniform, smooth, and morphologically stable. Furthermore, POM analysis showed that the LCE_3^{fiber} phase has a continuous surrounding around the PCL nanofibers. PCL-LCE_3^{fiber} (2:1) with an average diameter of ~659 nm was the most electrospinnable sample and produced smooth and uniform nanofibers without separation of the LCE phase.

3.5. Crystallinity and Transition Temperatures for LCE^{fiber} and PCL-LCE_3^{fiber} Samples. It has been widely also observed in this study that PCL, as a semicrystalline polymer,

https://doi.org/10.1021/acsomega.3c06528
ACS Omega 2023, 8, 46878−46891

has strong crystalline peaks positioned at Bragg angles of 2θ = 21.3 and 23.6°, which can be assigned to the crystalline planes of (1 0 0) and (2 0 0), respectively. In Figure 4b, the WAXS patterns of electrospun PCL (PCL^{fibers}), PCL-LCE_3^{fiber} (1:2), and LCE_3^{fiber} are shown, through which the crystallinity of the samples was estimated to be 49.34, 73.65, and 66.8%, respectively.[41] As depicted, the broad peak at 2θ = 41° and the broader peak compared to PCL^{fiber} at 2θ = 21.3° in the WAXS pattern for the PCL-LCE_3^{fiber} (2:1) sample showed the existence of a liquid crystalline phase related to LCE_3 [Figure 4c]. Also, the order parameters (S) for LCE_3^{fiber} and PCL-LCE_3^{fiber} (2:1) samples were 0.571 and 0.672, respectively, confirming the suitability of the electrospinning method to orient mesogenic chains compared to the cast film method.

Following this, the transition temperatures for LCE_3^{fiber} and PCL-LCE_3^{fiber} (2:1) nanofibers were evaluated by DSC. As shown in Figure 4d, the obtained thermograms (heating) for PCL^{fiber} and PCL-LCE_3^{fiber} (2:1) revealed endothermic peaks at 60.3 and 61.6 °C related to the melting points, respectively. Also, a more detailed observation of the PCL-LCE_3^{fiber} (2:1) thermogram depicted in the left corner of Figure 4d showed that the effect of the liquid crystalline phase presence appeared via the exothermic peak at 41.2 °C corresponding to the the LCE_3^{fiber} transition temperature (39.4 °C).

3.6. In Vitro Essay. In this study, the utilized LCE was based on a thermoresponsive mesogenic monomer in which T_{NI} was more than the biological temperature, leading to the anisotropic mesomorph of samples in biological environments. As reported previously, PC12 cell line as neuroblasma cells is highly responsive to surface patterning[42] and its performance in various developmental cell progressions can be simulated to peripheral nerve cells behavior. Optimized samples in terms of required properties, including LCE_3^{film}, LCE_3^{fiber}, neat PCL^{fiber}, and PCL-LCE_3^{fiber} (2:1) nanofibers, were prepared. The selection of the mentioned samples was due to the evaluation of two factors, including surface topography and presence of liquid crystalline phase on the cell-scaffold performance examined qualitatively and quantitatively.

3.6.1. Cell Viability, Adhesion, Differentiation, and Proliferation. The cell viability or cytotoxicity of the prepared samples was predominantly characterized by in vitro cell culture method to evaluate the behavior of PC12 cells during different conditions. For initial assessment of the prepared samples as a cell scaffold in vitro, an MTT assay was performed. In this line, PC12 cells were seeded with a constant cell number on LCE_3^{film}, LCE_3^{fiber}, PCL^{fiber}, and PCL-LCE_3^{fiber} (2:1) nanofibers to determine the extent of seeded cells viability, biocompatibility of specimens in biological environments, and their cytotoxicity. As shown in Figure 5a, the percentage of alive cells in each group was more than 80%, confirming that all prepared samples were cell viable, cell-compatible, and compatible with biological environments.

To study the differentiation's stimulatory effect of the mentioned samples, the expression of Nestin, an immature neuron, was analyzed by flow cytometry. Nestin expression on neuroblasts decreases during the differentiation procedure. Therefore, first, the cells were stained via anti-Nestin primary and fluorescein isothiocyanate (FITC) conjugated secondary antibodies, and their expressions were monitored. As depicted in Figure 5b, after PC12 cells were cultured on LCE_3^{film}, LCE_3^{fiber}, PCL^{fiber}, and PCL-LCE_3^{fiber} (2:1), Nestin expression significantly increased, indicating that all of the samples have a synergism effect on the differentiation process. Among them, the percentage of Nestin expression of cells cultured on PCL-LCE_3^{fiber} (2:1) nanofibers conspicuously differed from the other samples, confirming the ability of PCL-LCE_3^{fiber} (2:1) nanofibers to stimulate more strongly neuroblast cells' differentiation to neuron cells.

In the following, the expression of differentiated cultures to neuronal markers including Nestin, Map2, and Tubb3 was analyzed. For this purpose, PC12 cells were exposed to the prepared samples as cell scaffolds for 4 days while the expression of cells was determined by RT-PCR used as a control gene. As is seen in Figure 5c, the expression of all neural differentiation gene markers was increased significantly after 4 days of culture. By a qualitative comparison, it could be concluded that the expression of Map2 was the highest at the mRNA level for PCL-LCE_3^{fiber} (2:1) nanofibers and the Tubb3 level was also higher than that of PCL-LCE_3^{fiber} (2:1) nanofibers. The most important point was that all samples based on LCE on any type of topology were more capable of stimulating cells for differentiation, which shows that the presence of liquid crystalline phase alone could provide better conditions than scaffolds made up of common polymer nanofibers like PCL. However, the synergism effect of PCL in PCL-LCE_3^{fiber} (2:1) nanofibers compared to LCE_3^{fiber} nanofibers could be attributed to the electrospinnable essence of PCL, leading to preparation of more uniform LCE-contained fibers. Indeed, PCL nanofibers were the stable platform in which the photo-cross-linking procedure was completed. The fibrous topography and the nematic mesomorph of LCE sheath coated on PCL fibers were the highly effective factors confirming the suitability of the PCL-LCE_3^{fiber} (2:1) sample as a smart cell scaffold ($p < 0.05$).

3.6.2. Immunocytochemical Analysis of Cultured PC12 Cells. After 4 days of cell seeding, the cells were stained with anti-Nestin antibody, and their morphological properties were evaluated by an optical microscopy test to investigate the effect of topographical signals and scaffold topology on the developmental progression of PC12 cells. Figure 6 illustrates the optical microscopy images of PC12 cultured on LCE_3^{film}, LCE_3^{fiber}, PCL^{fiber}, and PCL-LCE_3^{fiber} (2:1) nanofibers. The influential effect of the liquid crystalline phase presence in LCE_3^{film}, LCE_3^{fiber}, and PCL-LCE^{fiber} (2:1) was obvious. The cultured cells on PCL nanofibers [Figure 6g–i] spread inadequately with round shapes compared with the other samples. In contrast, the cells seeded on the LCE_3^{film} [Figure 6a–c] had more expanded morphologies, even though the mentioned sample did not have nanofibrous topology as the physical cell signals. By comparing the cell numbers and topologies, it was concluded that fibrous topologies were able to guide the cells more compared to LCE_3^{fiber} and PCL-LCE_3^{fibers} (2:1) nanofibers Figure 6d–f,6j–l. As mentioned before, induction of topographical cues to the biological cells motivates them to form efficient cell–cell and cell–substrate interactions. This phenomenon confirmed the liquid crystal phase effectiveness and demonstrated how the LCE-based materials themselves can give favorable interactions helping the pathway of cellular differentiation.[12] Also, other research groups proved that LCE self-assembled structures can be exploited for the alignment of different cell lines due to the spontaneous surface-induced pattern formation.[43]

3.7. Active Defects in PC12 Cells. The investigation of cellular organization in various cell lines such as fibroblast cells as well as cells in the cat's visual cortex demonstrated that cells have a particular point termed the pinwheel structure.

https://doi.org/10.1021/acsomega.3c06528
ACS Omega 2023, 8, 46878–46891

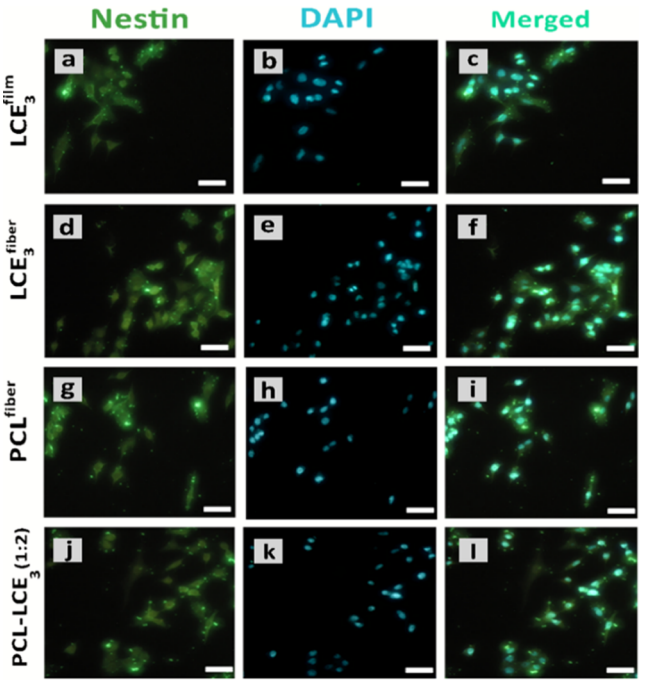

Figure 6. Images of PC12 cells cultured on (a–c) LCE_3^{film}, (d–f) nanofibrous LCE_3^{fiber}, (g–i) PCL^{fiber}, and (j–l) PCL-LCE_3^{fiber} (2:1) nanofibrous samples stained with anti-Nestin antibody.

Evidently, presence of the mentioned points is vital for the organization of neurons in the visual cortex.[44] Defects with the topological charges of +1/2 and −1/2 are commonly observed in cell cultures and have therefore been the subject of many studies. On the other hand, defects with integer charges of +1 and −1 are not typically observed in flat layers and have received less attention. However, these types of defects are still present in living systems in various forms. There are many examples of fibers forming topological defects with +1 charge, either with azimuthal or with radial alignment, such as those around the optic nerve and at the tumor-stromal interface.[9,14] In this line, the flow fields and topological defects of PC12 cells seeded on LCE_3^{film}, LCE_3^{fiber}, PCL^{fibers}, and PCL-LCE^{fiber} (2:1) nanofibers were characterized over a period of time. Figure 7 shows the flow fields of PC12 cells seeded on the mentioned samples 15, 45, and 90 min after culture. In all samples, cell behavior showed that the biological cells did not have linear motion during the culturing. They presented a dynamic motion that was affected by the enamoring cells. When the cell density exceeded, cells were ordered in a special manner in which the monolayer of the cells was divided into many fractures, in which the cells were directed toward a particular director vector. The flow of cells with a nonparallel director vector at a point creates singularities, which are actuating agents for biological cells to grow, differentiate, and proliferate. These disclinations act as topographical cues causing

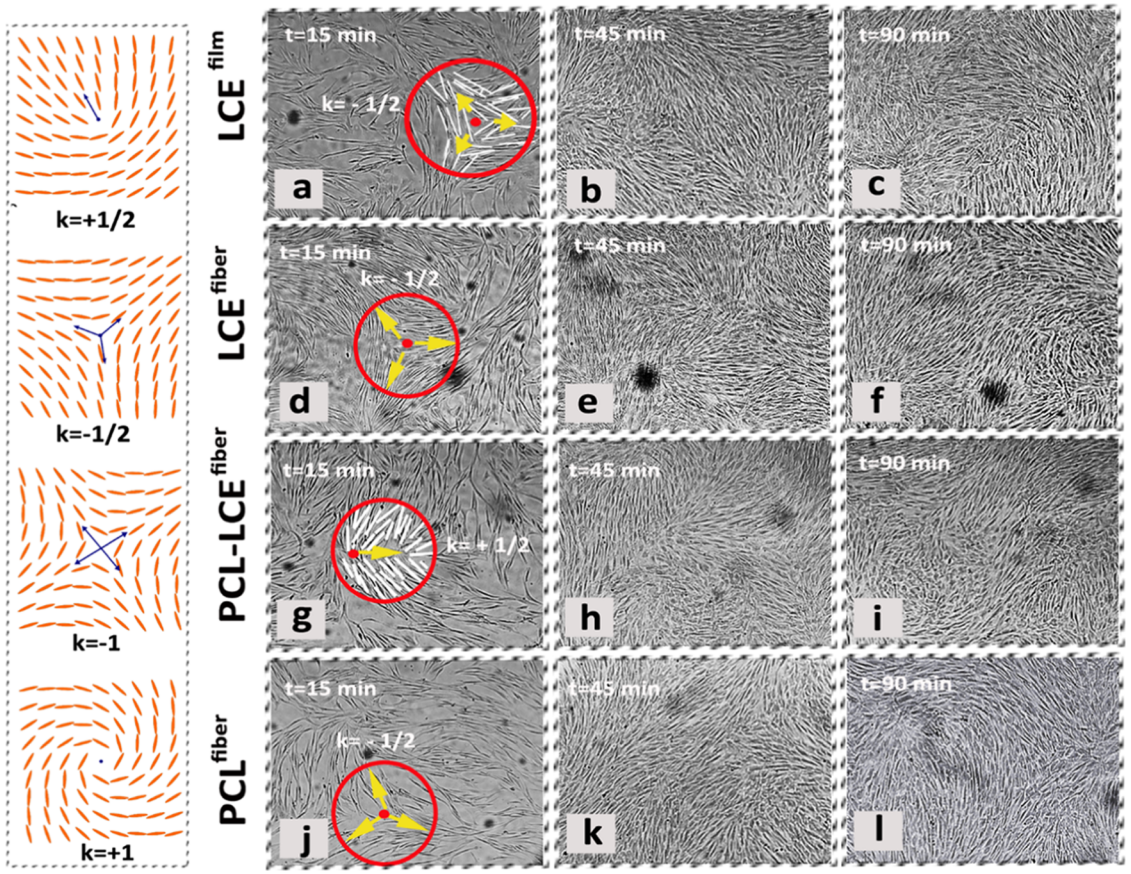

Figure 7. Illustration of cells' topological defects at different times after cell culture: (a) Pc12 cells cultured on LCE^{film} at t = 15, (b) PC12 cells cultured on LCE^{film} at t = 45, (c) PC12 cells cultured on LCE^{film} at t = 90, (d) PC12 cells cultured on LCE^{fiber} at t = 15, (e) PC12 cells cultured on LCE^{fiber} at t = 45, (f) PC12 cells cultured on LCE^{fiber} at t = 90, (g) PC12 cells cultured on PCL-LCE^{fiber} at t = 15, (h) PC12 cells cultured on PCL-LCE^{fiber} at t = 45, (i) PC12 cells cultured on PCL-LCE^{fiber} at t = 90, (j) PC12 cells cultured on PCL^{fiber} at t = 15, (k) PC12 cells cultured on PCL^{fiber} at t = 30, and (l) PC12 cells cultured on PCL^{fiber} at t = 90.

https://doi.org/10.1021/acsomega.3c06528
ACS Omega 2023, 8, 46878−46891

regulation of cells, self-organization, dynamic movements, and cell−cell interactions. As shown in Figure 7a−c, the seeded cells on LCE_3^{film} were able to form a singularity point similar to liquid crystal defects. Indeed, comet-like shapes directed toward the flow of cultured cells were observed for all samples, confirming that the formation of a special flow field and nematic orientational order would take place independent of the substrate type. However, the type of substrate was influential on the speed of formation and number of topological defects. Figure 7a,d,g indicates that topological defects of $k = \pm 1/2$, which are commonly observed in active nematics, especially in biological cell lines, were formed even after 15 min [Figure 7a,g]. Comparing the cells' orientational order in LCE_3^{film} and PCL^{fiber} indicates that in spite of the nanofibrous topology of PCL^{fiber} the density of the formed defects in LCE_3^{film} was 2 times more than that in PCL^{fiber} nanofibers. This phenomenon proved that though LCE_3^{film} had a continuous surface and noninterconnected topology, the topographical cues induced by the liquid crystalline substrate were more effectual compared to fibrous topology. Cells cultured on PCL^{fiber} were oriented more compared to seeded cells on the LCE_3^{film} sample due to the fibrous topographical cue, which motivates the cells to orient alongside the PCL fibers. However, PC12 cells on LCE_3^{film} tended to organize themselves more due to the high defect density followed by higher differentiation and proliferation, which were confirmed in Figure 5 and plotted in Figure 7b,c,k,l. Comparison of cell behavior in all samples at $t = 15$ in Figure 7d,g showed obviously that on the PC12 cells cultured on PCL-LCE^{fiber} (2:1) and LCE_3^{fiber} nanofibrous scaffolds, topological defects emerged clearly compared to PCL^{fiber} nanofibers and LCE_3^{fiilm} [Figure 7a, j]. Figure 7b,c,k,l showed that after a while all samples were capable of topological effect formation, but the number of defects for LCE_3^{film}, LCE_3^{fiber}, PCL^{fibers}, and PCL-LCE^{fiber} (2:1) nanofibers was 190, 256, 123, and 330 in an area of 1 μm^2, respectively. By comparing the mentioned amounts for LCE_3^{film} and PCL^{fibers} it was concluded that despite PCL^{fibers} nanofibers possessing a fibrous topology, the existence of LCEs, even with the topology of the film, was more effective to form topological defects and guide cells. This fact is evident when considering the densities of PCL^{fibers} and PCL-LCE^{fiber} (2:1) nanofibers. The existence of LCE could increase the number of defects approximately 2.7 times. The high amounts of topological defects in PCL-LCE^{fiber} (2:1) and LCE_3^{fiber} nanofibers confirmed the fact that these singularity points enhance the topographical signals toward the cells and that the PCL-LCE^{fiber} (2:1) nanofibrous scaffold is an applicable substrate for regeneration of peripheral nerve tissues due to its higher compatibility, better differentiation, and more proliferation of PC12v cells.

4. CONCLUSIONS

Since liquid crystal elastomers are inherently able to regulate biological cells, the effect of these polymers on PC12 cells was investigated. Studies on the mechanical, morphological, and anisotropic properties showed that these materials are able to improve the dynamic intracellular interactions of PC12 cells in the processes of growth, reproduction, and differentiation. Studies on the mechanical, morphological, and anisotropic properties showed that these materials are able to improve the dynamic processes of PC12 cells in the processes of growth, proliferation, and differentiation. In order to investigate the effect of scaffold topology on the formation of topological defects, four types of samples as cell scaffolds, including LCE^{film}, LCE^{fiber}, PCL-LCE^{fiber}, and $PCL^{nanofibers}$, were investigated on a molecular level. The obtained results proved that all samples were biologically compatible with cells and nontoxic. Moreover, the PCL-LCE^{fiber} scaffold showed a better performance compared to the other samples, and the conspicuous effect of the liquid crystalline phase presence in PCL-LCE^{fiber} led to considering it as an efficient alternative of typical fibrous scaffolds.

■ ASSOCIATED CONTENT

Supporting Information

The Supporting Information is available free of charge at https://pubs.acs.org/doi/10.1021/acsomega.3c06528.

FE-SEM images of electrospun LCE_3^{fiber} nanofibers at different voltages Mw amounts for LCE^{fiber} samples (PDF)

■ AUTHOR INFORMATION

Corresponding Author

Payam Zahedi − *Nano-Biopolymers Research Laboratory, School of Chemical Engineering, College of Engineering, University of Tehran, Tehran 1417613131, Iran;* orcid.org/0000-0001-6636-4534; Phone: +98 (21) 61112247; Email: phdzahedi@ut.ac.ir; Fax: +98 (21) 66957784

Author

Mahshid Fallah-Darrehchi − *Nano-Biopolymers Research Laboratory, School of Chemical Engineering, College of Engineering, University of Tehran, Tehran 1417613131, Iran*

Complete contact information is available at: https://pubs.acs.org/10.1021/acsomega.3c06528

Notes

The authors declare no competing financial interest.

■ ACKNOWLEDGMENTS

The authors would like to express their sincere thanks to the Research Council of University of Tehran for the experimental services.

■ REFERENCES

(1) Li, Y.; Liu, T.; Ambrogi, V.; Rios, O.; Xia, M.; He, W.; Yang, Z. Liquid crystalline elastomers based on click chemistry. *ACS Appl. Mater. Interfaces* **2022**, *14* (13), 14842−14858.

(2) Ustunel, S.; Sternbach, S.; Prévôt, M. E.; Freeman, E. J.; McDonough, J. A.; Clements, R. J.; Hegmann, E. 3D Co-culturing of human neuroblastoma and human oligodendrocytes, emulating native tissue using 3D porous biodegradable liquid crystal elastomers. *J. Appl. Polym. Sci.* **2023**, *140*, No. e53883.

(3) Krause, S.; Dersch, R.; Wendorff, J. H.; Finkelmann, H. Photocrosslinkable liquid crystal main-chain polymers: thin films and electrospinning. *Macromol. Rapid Commun.* **2007**, *28* (21), 2062−2068.

(4) Kularatne, R. S.; Kim, H.; Boothby, J. M.; Ware, T. H. Liquid crystal elastomer actuators: Synthesis, alignment, and applications. *J. Polym. Sci., Part B: Polym. Phys.* **2017**, *55* (5), 395−411.

(5) Ohm, C.; Brehmer, M.; Zentel, R. Liquid crystalline elastomers as actuators and sensors. *Adv. Mater.* **2010**, *22* (31), 3366−3387.

(6) Ula, S. W.; Traugutt, N. A.; Volpe, R. H.; Patel, R. R.; Yu, K.; Yakacki, C. M. Liquid crystal elastomers: an introduction and review of emerging technologies. *Liquid Cryst. Rev.* **2018**, *6* (1), 78−107.

(7) Li, G.-Z.; Randev, R. K.; Soeriyadi, A. H.; Rees, G.; Boyer, C.; Tong, Z.; Davis, T. P.; Becer, C. R.; Haddleton, D. M. Investigation into thiol-(meth) acrylate Michael addition reactions using amine and phosphine catalysts. *Polym. Chem.* **2010**, *1* (8), 1196−1204.
(8) Li, Y.; Xiao, Y.; Liu, C. The horizon of materiobiology: a perspective on material-guided cell behaviors and tissue engineering. *Chem. Rev.* **2017**, *117* (5), 4376−4421.
(9) Fallah-Darrehchi, M.; Zahedi, P.; Harirchi, P.; Abdouss, M. Performance of Liquid Crystalline Elastomers on Biological Cell Response: A Review. *ACS Appl. Polym. Mater.* **2023**, *5*, 1076−1091, DOI: 10.1021/acsapm.2c01599.
(10) Rojas-Rodríguez, M.; Fiaschi, T.; Mannelli, M.; Mortati, L.; Celegato, F.; Wiersma, D. S.; Parmeggiani, C.; Martella, D. Cellular Contact Guidance on Liquid Crystalline Networks with Anisotropic Roughness. *ACS Appl. Mater. Interfaces* **2023**, *15* (11), 14122−14130, DOI: 10.1021/acsami.2c22892.
(11) Doostmohammadi, A.; Ladoux, B. Physics of liquid crystals in cell biology. *Trends Cell Biol.* **2022**, *32* (2), 140−150.
(12) Martella, D.; Mannelli, M.; Squecco, R.; Garella, R.; Idrizaj, E.; Antonioli, D.; Laus, M.; Wiersma, D. S.; Gamberi, T.; Paoli, P.; et al. Cell instructive Liquid Crystalline Networks for myotube formation. *Iscience* **2021**, *24* (9), No. 103077.
(13) Babakhanova, G.; Turiv, T.; Guo, Y.; Hendrikx, M.; Wei, Q.-H.; Schenning, A. P.; Broer, D. J.; Lavrentovich, O. D. Liquid crystal elastomer coatings with programmed response of surface profile. *Nat. Commun.* **2018**, *9* (1), No. 456.
(14) Endresen, K. D.; Kim, M.; Pittman, M.; Chen, Y.; Serra, F. Topological defects of integer charge in cell monolayers. *Soft Matter* **2021**, *17* (24), 5878−5887.
(15) Martella, D.; Paoli, P.; Pioner, J. M.; Sacconi, L.; Coppini, R.; Santini, L.; Lulli, M.; Cerbai, E.; Wiersma, D. S.; Poggesi, C.; et al. Liquid crystalline networks toward regenerative medicine and tissue repair. *Small* **2017**, *13* (46), No. 1702677.
(16) Saw, T. B. *The Role of Mechanics and Collective Cell Constraints in Epithelial Cell Death and Extrusion*; National University of Singapore: Singapore, 2017.
(17) Saw, T. B.; Doostmohammadi, A.; Nier, V.; Kocgozlu, L.; Thampi, S.; Toyama, Y.; Marcq, P.; Lim, C. T.; Yeomans, J. M.; Ladoux, B. Topological defects in epithelia govern cell death and extrusion. *Nature* **2017**, *544* (7649), 212−216.
(18) Chung, W.-J.; Merzlyak, A.; Yoo, S. Y.; Lee, S.-W. Genetically engineered liquid-crystalline viral films for directing neural cell growth. *Langmuir* **2010**, *26* (12), 9885−9890.
(19) Kawaguchi, K.; Kageyama, R.; Sano, M. Topological defects control collective dynamics in neural progenitor cell cultures. *Nature* **2017**, *545* (7654), 327−331.
(20) Mehata, A. K.; Dehari, D.; Gupta, A.; Rabin, D. C.; Miya, A. Multifunctional liquid crystal nanoparticles for cancer therapy. *Curr. Nanomater.* **2021**, *6* (1), 4−16.
(21) Bera, T.; Freeman, E. J.; McDonough, J. A.; Clements, R. J.; Aladlaan, A.; Miller, D. W.; Malcuit, C.; Hegmann, T.; Hegmann, E. Liquid crystal elastomer microspheres as three-dimensional cell scaffolds supporting the attachment and proliferation of myoblasts. *ACS Appl. Mater. Interfaces* **2015**, *7* (26), 14528−14535.
(22) Liu, F.; Xu, J.; Wu, L.; Zheng, T.; Han, Q.; Liang, Y.; Zhang, L.; Li, G.; Yang, Y. The influence of the surface topographical cues of biomaterials on nerve cells in peripheral nerve regeneration: a review. *Stem Cells Int.* **2021**, *2021*, No. 8124444, DOI: 10.1155/2021/8124444.
(23) Xue, W.; Shi, W.; Kong, Y.; Kuss, M.; Duan, B. Anisotropic scaffolds for peripheral nerve and spinal cord regeneration. *Bioact. Mater.* **2021**, *6* (11), 4141−4160.
(24) McCracken, J. M.; Tondiglia, V. P.; Auguste, A. D.; Godman, N. P.; Donovan, B. R.; Bagnall, B. N.; Fowler, H. E.; Baxter, C. M.; Matavulj, V.; Berrigan, J. D.; White, T. J. Microstructured Photopolymerization of Liquid Crystalline Elastomers in Oxygen-Rich Environments. *Adv. Funct. Mater.* **2019**, *29* (40), No. 1903761.
(25) Ube, T.; Tsunoda, H.; Kawasaki, K.; Ikeda, T. Photoalignment in polysiloxane liquid-crystalline elastomers with rearrangeable networks. *Adv. Opt. Mater.* **2021**, *9* (9), No. 2100053.
(26) Martinez, A. M.; Cox, L. M.; Killgore, J. P.; Bongiardina, N. J.; Riley, R. D.; Bowman, C. N. Permanent and reversibly programmable shapes in liquid crystal elastomer microparticles capable of shape switching. *Soft Matter* **2021**, *17* (3), 467−474.
(27) Lin, X.; Saed, M. O.; Terentjev, E. M. Continuous spinning aligned liquid crystal elastomer fibers with a 3D printer setup. *Soft Matter* **2021**, *17* (21), 5436−5443.
(28) Sharma, A.; Lagerwall, J. P. Electrospun composite liquid crystal elastomer fibers. *Materials* **2018**, *11* (3), No. 393.
(29) Ambulo, C. P.; Burroughs, J. J.; Boothby, J. M.; Kim, H.; Shankar, M. R.; Ware, T. H. Four-dimensional printing of liquid crystal elastomers. *ACS Appl. Mater. Interfaces* **2017**, *9* (42), 37332−37339.
(30) Bandyopadhyay, A.; Bose, S.; Das, S. 3D printing of biomaterials. *MRS Bull.* **2015**, *40* (2), 108−115.
(31) Yuan, C.; Roach, D. J.; Dunn, C. K.; Mu, Q.; Kuang, X.; Yakacki, C. M.; Wang, T.; Yu, K.; Qi, H. J. 3D printed reversible shape changing soft actuators assisted by liquid crystal elastomers. *Soft Matter* **2017**, *13* (33), 5558−5568.
(32) Chen, H.-Q.; Wang, X.-Y.; Bisoyi, H. K.; Chen, L.-J.; Li, Q. Liquid crystals in curved confined geometries: Microfluidics bring new capabilities for photonic applications and beyond. *Langmuir* **2021**, *37* (13), 3789−3807.
(33) Fleischmann, E. K.; Forst, F. R.; Zentel, R. Liquid-Crystalline Elastomer Fibers Prepared in a Microfluidic Device. *Macromol. Chem. Phys.* **2014**, *215* (10), 1004−1011.
(34) He, Q.; Wang, Z.; Wang, Y.; Wang, Z.; Li, C.; Annapooranan, R.; Zeng, J.; Chen, R.; Cai, S. Electrospun liquid crystal elastomer microfiber actuator. *Sci. Rob.* **2021**, *6* (57), No. eabi9704.
(35) Kim, D. K.; Hwang, M.; Lagerwall, J. P. Liquid crystal functionalization of electrospun polymer fibers. *J. Polym. Sci., Part B: Polym. Phys.* **2013**, *51* (11), 855−867.
(36) Krause, S.; Zander, F.; Bergmann, G.; Brandt, H.; Wertmer, H.; Finkelmann, H. Nematic main-chain elastomers: Coupling and orientational behavior. *C. R. Chim.* **2009**, *12* (1−2), 85−104.
(37) Bayat, G.; Fallah-Darrehchi, M.; Zahedi, P.; Moghaddam, A. B.; Ghaffari-Bohlouli, P.; Jafari, H. Kiwi extract-incorporated poly (ε-caprolactone)/cellulose acetate blend nanofibers for healing acceleration of burn wounds. *J. Biomater. Sci., Polym. Ed.* **2023**, *34* (1), 72−88.
(38) Yin, L.; Han, L.; Ge, F.; Tong, X.; Zhang, W.; Soldera, A.; Zhao, Y. A Novel Side-Chain Liquid Crystal Elastomer Exhibiting Anomalous Reversible Shape Change. *Angew. Chem.* **2020**, *132* (35), 15241−15246.
(39) Wang, Z.; Tian, H.; He, Q.; Cai, S. Reprogrammable, reprocessible, and self-healable liquid crystal elastomer with exchangeable disulfide bonds. *ACS Appl. Mater. Interfaces* **2017**, *9* (38), 33119−33128.
(40) Lee, Y.; Choi, S.; Kang, B.-G.; Ahn, S.-k. Effect of isomeric amine chain extenders and crosslink density on the properties of liquid crystal elastomers. *Materials* **2020**, *13* (14), No. 3094.
(41) Goudarzi, Z. M.; Behzad, T.; Ghasemi-Mobarakeh, L.; Kharaziha, M.; Enayati, M. S. Structural and mechanical properties of fibrous poly (caprolactone)/gelatin nanocomposite incorporated with cellulose nanofibers. *Polym. Bull.* **2020**, *77*, 717−740.
(42) Fallah-Darrehchi, M.; Zahedi, P.; Safarian, S.; Ghaffari-Bohlouli, P.; Aeinehvand, R. Conductive conduit based on electrospun poly (L-lactide-co-D, L-lactide) nanofibers containing 4-aminopyridine-loaded molecularly imprinted poly (methacrylic acid) nanoparticles used for peripheral nerve regeneration. *Int. J. Biol. Macromol.* **2021**, *190*, 499−507.
(43) Turiv, T.; Krieger, J.; Babakhanova, G.; Yu, H.; Shiyanovskii, S. V.; Wei, Q.-H.; Kim, M.-H.; Lavrentovich, O. D. Topology control of human fibroblast cells monolayer by liquid crystal elastomer. *Sci. Adv.* **2020**, *6* (20), No. eaaz6485.

https://doi.org/10.1021/acsomega.3c06528
ACS Omega 2023, 8, 46878−46891

(44) Doostmohammadi, A.; Ignés-Mullol, J.; Yeomans, J. M.; Sagués, F. Active nematics. *Nat. Commun.* **2018**, *9* (1), No. 3246.

https://doi.org/10.1021/acsomega.3c06528
ACS Omega 2023, 8, 46878−46891